Design, Synthesis, and Characterization of Metal-Organic Frameworks for Enhanced Sorption of Chemical Warfare Agent Simulants—Supporting Information

Jonathan P. Ruffley[†,#], Isabella Goodenough[‡,#], Tian-Yi Luo[§,#], Melissandre Richard[‡,⊥], Eric Borguet[‡], Nathaniel L. Rosi[†,§]*, J. Karl Johnson[†]**

[†] Department of Chemical and Petroleum Engineering, University of Pittsburgh, Pittsburgh, Pennsylvania 15261, United States of America

[‡] Department of Chemistry, Temple University, Philadelphia, Pennsylvania 19122, United States of America

[§] Department of Chemistry, University of Pittsburgh, Pittsburgh, Pennsylvania 15261, United States of America

[#]Authors contributed equally to this work

Table S1. Convergence criteria for ORCAgeometry optimizations. G is the gradient and D is displacement.

type	tolerance
E	5×10^{-6} Eh
RMSG	1×10^{-4} Eh/bohr
Max G	3×10^{-4} Eh/bohr
RMSD	2×10^{-3} bohr
Max D	4×10^{-3} bohr

Table S2. Gaussian 09 cluster binding energies between DMMP and ligand models for UiO-67, with counterpoise corrected energies. While the counterpoise correction energies result in substantial error of over 50% for the weakest binding energies, applying the correction does not change the relative order of binding strength.

interaction pair	ΔE_{bind} (kJ/mol)	E_{CP} (kJ/mol)	$\Delta E_{bind,CP}$ (kJ/mol)
DMMP + aniline	-25.33	3.19	-22.14
DMMP + thiophenol	-20.74	3.25	-17.49
DMMP + nitrobenzene	-17.88	3.57	-14.31
DMMP + bromobenzene	-11.31	2.60	-8.71
DMMP + toluene	-10.70	2.84	-7.86
DMMP + chlorobenzene	-9.80	2.80	-7.00
DMMP + phenyl azide	-8.32	2.96	-5.36
DMMP + benzene	-6.36	2.50	-3.85

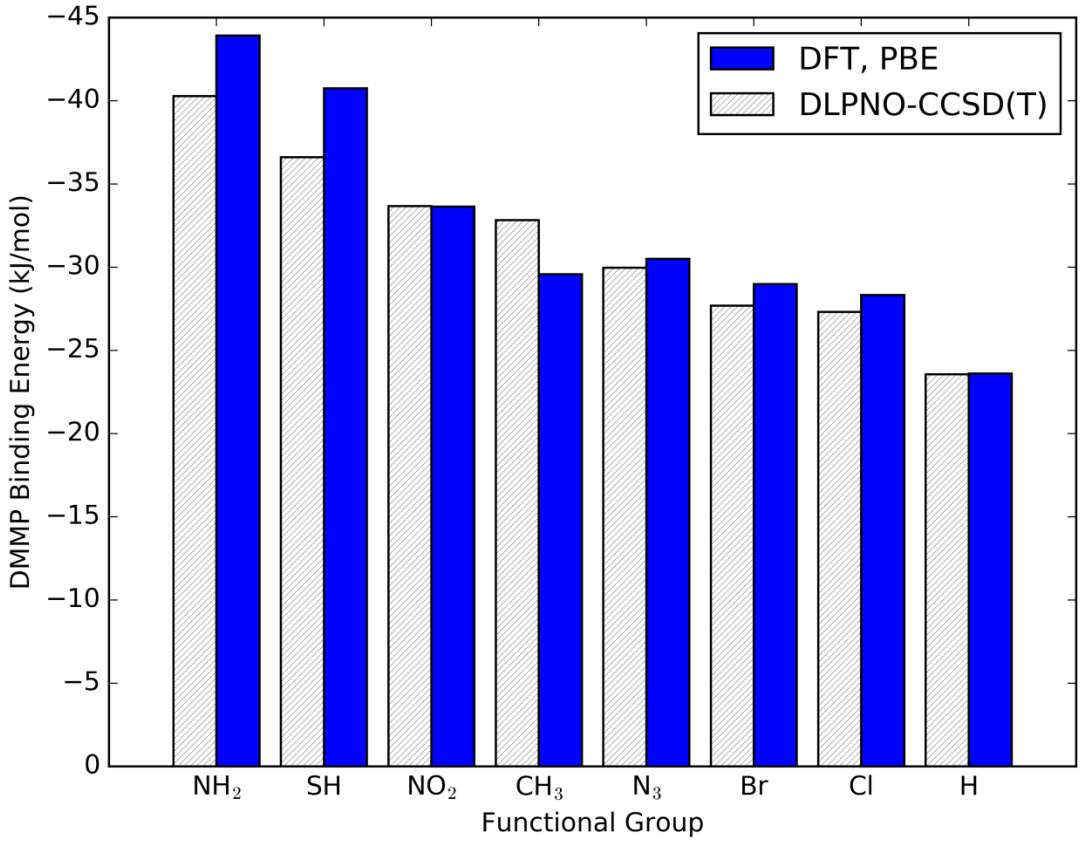

Figure S1. Binding energies calculated between DMMP and functional groups using DFT with the PBE functional and DLPNO-CCSD(T). Orca[1] was used for all calculations. The only change in the relative binding strength is the N_3 functionalized ligand. However, the energies in question differ by less than 1 kJ/mol, making this change in relative binding strength inconsequential.

Primitive cell optimizations, done with CP2K 4.1,[2-4] required selection of both cutoff and relative cutoff at converged values. Convergence was defined as no change in the single point energy to 1×10^{-5} hartree. Converged values were 400 rydberg cutoff and 50 rydberg relative cutoff.

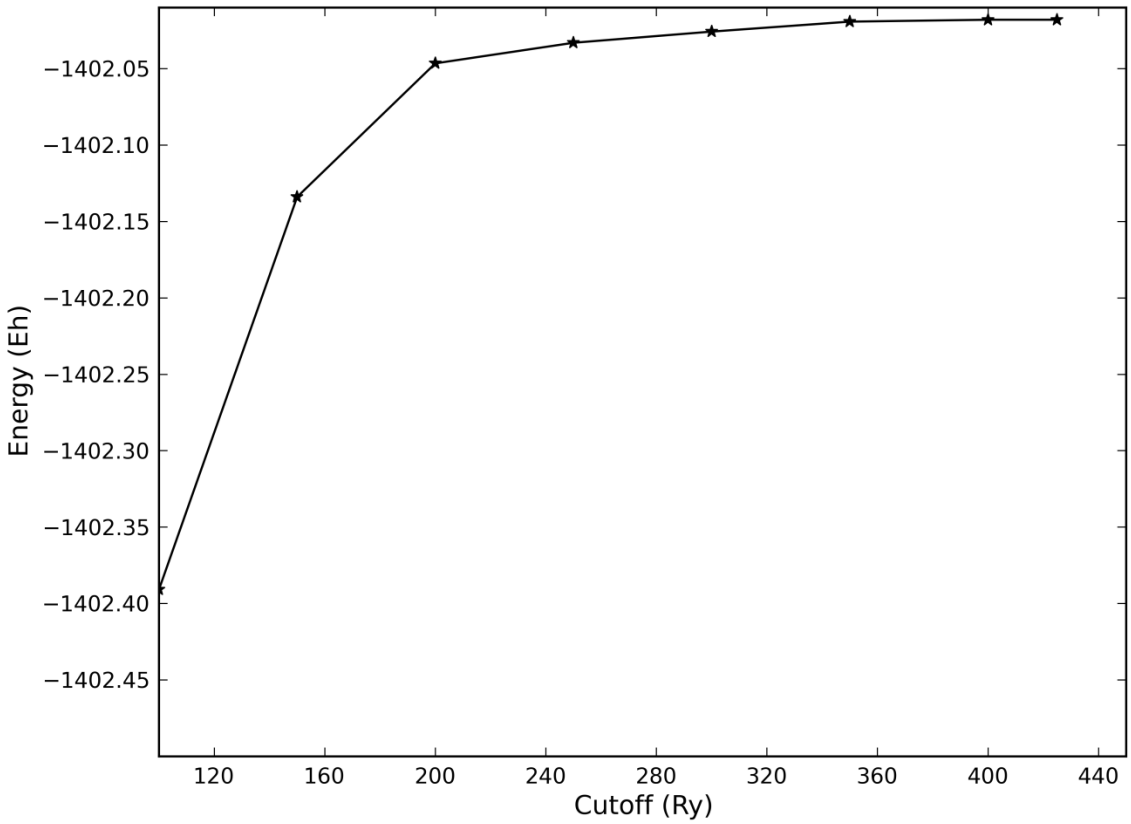

Figure S2. Convergence of the cutoff for UiO-67 using CP2K.

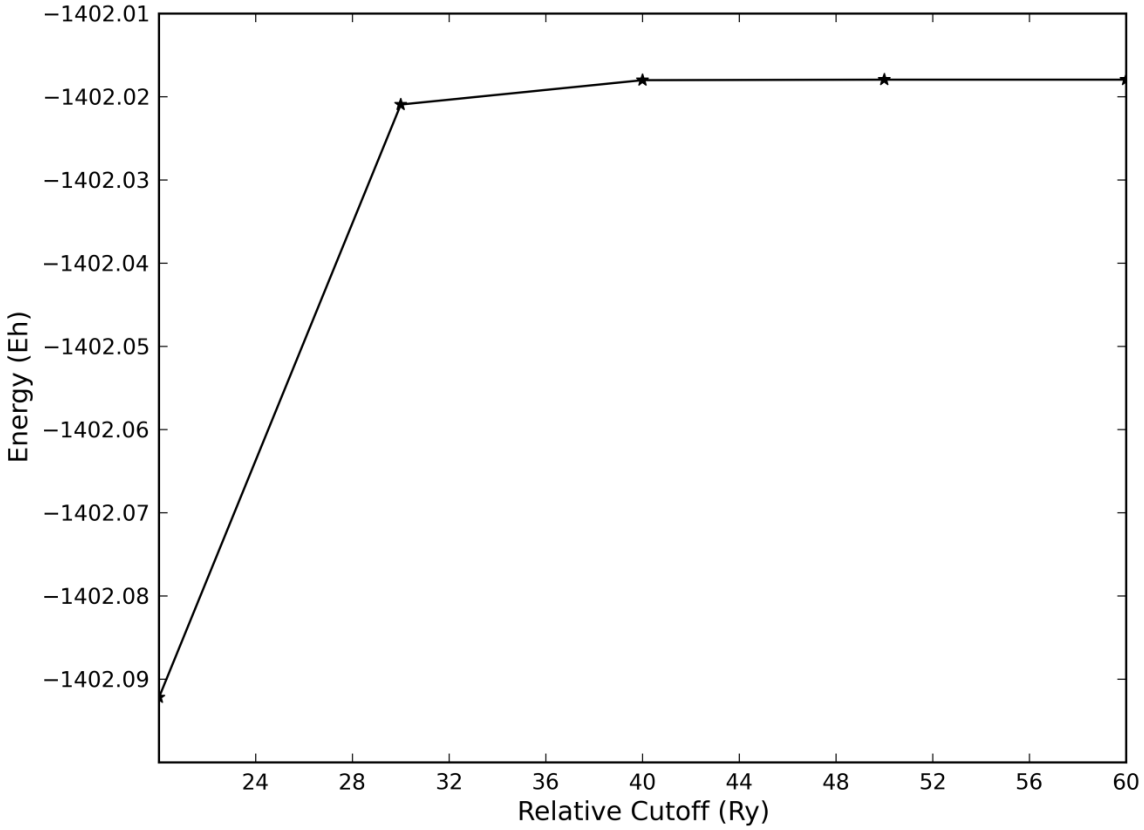

Figure S3. Convergence of the relative cutoff for UiO-67 using CP2K.

Synthesis of **2-amino-1,1'-biphenyl-4,4'-dicarboxylic acid**

2-Amino-1,1'-biphenyl-4,4'-dicarboxylic acid was synthesized according to literature conditions.[5]

Synthesis of **2-methyl-1,1'-biphenyl-4,4'-dicarboxylic acid**

2-Methyl-1,1'-biphenyl-4,4'-dicarboxylic acid was synthesized according to literature conditions.[6]

Synthesis of **UiO-67 (5-60)** $Zr_6(OH)_4O_4(C_{14}H_8O_4)_{5.6}(OH)_{0.8}(H_2O)_{0.8}$

A stock solution of 1,1'-biphenyl-4,4'-dicarboxylic acid (H_2-BPDC) (0.04 M) in DMF was first prepared by dissolving BPDC (106.6 mg, 0.44 mmol) in DMF (11 mL) in a loosely capped 20 mL vial. To facilitate the dissolution of H_2-BPDC, the vial was heated on a ceramic stir plate at ~150˚C until clear solution was formed. The solution was cooled to room temperature. To a flame-dried 250 mL round-bottom flask was added $ZrCl_4$ (93.2 mg, 0.4 mmol), DMF (43 mL) and acetic acid (7 mL). The reaction mixture was sonicated for 1 min before the flask was capped by a septum and heated in oil bath at 120˚C for 10 min. 0.04 M BPDC stock solution (10 mL, 0.4 mmol) was then added to the reaction mixture. The mixture was heated in oil bath at 120˚C for 5 hours to yield cloudy suspension. After cooling to room temperature, the reaction mixture was centrifuged at 3000 rpm for 15 min to yield white precipitate. The precipitate was washed with fresh DMF (120 mL, 3x). Calc: C,45.88; H, 2.51; N, 0.00; Found: C, 45.72; H, 2.04; N, 0.00.

Synthesis of **UiO-67-CH_3** $Zr_6O_4(OH)_4(C_{15}H_{10}O_4)_{5.2}(OH)_{1.6}(H_2O)_{1.6}$

To a flame-dried 250 mL round-bottom flask was added $ZrCl_4$ (46.6 mg, 0.2 mmol), DMF (50 mL) and acetic acid (2.5 mL). The reaction mixture was sonicated for 1 min before the flask was capped by a septum and heated in oil bath at 100˚C for 10 min. 2-methyl-1,1'-biphenyl-4,4'-dicarboxylic acid (H_2-CH_3-BPDC) (51.2 mg, 0.2 mmol) was then added to the reaction mixture. The mixture was sonicated for 1 min and heated in oil bath at 100˚C for 14.5 hours to yield a cloudy suspension. After cooling to room temperature, the reaction mixture was centrifuged at 3000 rpm for 15 min to yield white precipitate. The precipitate was washed with fresh DMF (120 mL, 3x). Calc: C, 45.53; H, 2.98; N, 0.00; Found: C, 45.26; H, 2.52; N, 0.19.

Synthesis of **UiO-67-NH_2** $Zr_6O_4(OH)_4(C_{14}NH_9O_4)_{5.5}(OH)(H_2O)$

0.4 M solution of $Zr(O^nPr)_4$ in CH_3COOH was prepared by mixing $Zr(O^nPr)_4$ 70 wt. % in 1-propanol (187.2 mg, 0.04 mmol) with CH_3COOH (1 mL). To a 40 mL Pyrex vial were added acetic acid (1.2 mL) To a 40 mL Pyrex vial were added in sequence CH_3COOH (1.2 mL), 0.4 M $Zr(n\text{-}OPr)_4$ solution (0.3 mL, 0.12 mmol), DMF (24 mL) and 2-amino-1,1'-biphenyl-4,4'-dicarboxylic acid (H_2-NH_2-BPDC) (30.9 mg, 0.12 mmol). After sonication for 1 min, the tightly capped vial was heated at 65˚C in an isothermal oven for 16 h to yield a turbid yellow suspension. The mixture was centrifuged at 3000 rpm for 15 min to obtain yellow precipitate. The precipitate was washed with fresh DMF (120 mL, 3x). Calc: C,43.66; H, 2.69; N, 3.64; Found: C,43.24; H, 2.32; N, 3.52.

Development of DMMP Potential

The united atom DMMP potential was described by eq (S1), where the bond contribution was determined by eq (S2), the angle contribution was determined by eq (S3), and the dihedral torsion contribution was determined by eq (S4).

$$V = V_{bond} + V_{bend} + V_{torsion} \quad (S1)$$

$$V_{bond} = \frac{1}{2} K_r (r - r_0) \quad (S2)$$

$$V_{angle} = \frac{1}{2} K_\theta (\theta - \theta_0) \quad (S3)$$

$$V_{torsion} = \frac{1}{2} K_\varphi [\{1 - \cos\{\mathrm{m}(\varphi - \varphi_0)\}] \quad (S4)$$

QuickFF[7] parameters were generated using standard accuracy and output from a VASP[8-11] vibrational calculation.

It is expected that the bonded potential terms will be widely applicable for force-field based simulations of DMMP, as QuickFF has been shown to be robust and generally applicable to a variety of molecules.[7] While the Lennard-Jones and electrostatic parameters developed here were not tested over a range of states for accuracy, the goal of this work is not to develop such a widely robust model. Rather, the intention is to produce a model that will give a reasonable prediction of the behavior of DMMP. Here, a density of 1143 kg/m^3 at 298 K and 1 atm is obtained, while the literature value at these conditions is 1145 kg/m^3.

Table S3. Simulation parameters for LAMMPS NPT to fit an atomic potential for DMMP.

cutoff	14 Å
molecules	155
equilibration steps	100,000
production steps	500,000
timestep	0.25 fs

Table S4. Simulation parameters for RASPA NPT to fit an atomic potential for DMMP.

cutoff	14 Å
molecules	155
equilibration cycles	100,000
production cycles	300,000

Table S5. Lennard-Jones 12-6 potential parameters and atomic charges used to calculate non-bonded contributions to the potential for the DMMP molecule.

atom	ε (kcal/mol)	σ (Å)	q (e)
CH_3(-O)	0.169	3.75	0.135
CH_3(-P)	0.169	3.75	0.021
O	0.095	2.80	-0.360
O(=P)	0.137	3.05	-0.691
P	0.149	4.00	1.120

Table S6. Bond stretch parameters for the DMMP molecule. Parameters were used with eq (S2) to calculate the bond stretch contribution to the potential.

bond	K_r (kcal/(mol*Å))	r_0 (Å)
CH_3 - O	342.22	1.469
CH_3 - P	222.1	1.801
O - P	342.31	1.633
O = P	667.99	1.47

Table S7. Bond-bend parameters for the DMMP molecule. Parameters were used with eq (S3) to calculate the angle contribution to the potential.

angle	K_θ (kcal/(mol*degree))	θ_0 (degree)
CH_3 - O - P	56.451	111.13
CH_3 - P - O	87.035	101.9
CH_3 - P = O	71.5	118.7
O - P - O	88.928	106.08
O - P = O	77.731	113.55

Table S8. Dihedral torsion parameters for the DMMP molecule. Parameters were used with eq (S4) to calculate the dihedral torsion contribution to the potential.

torsion	K_φ (kcal/(mol*degree))	m	φ_0 (degree)
CH_3 - O - P - CH_3	0.7192	3	0
CH_3 - O - P - O	0.0809	3	0
CH_3 - O - P = O	0.6096	3	0

Table S9. Helium void fractions calculated for each MOF were used to calculate excess adsorption isotherms in RASPA.

MOF	He void fraction
UiO-67	0.6793
UiO-67-NH_2	0.6429
UiO-67-CH_3	0.6289

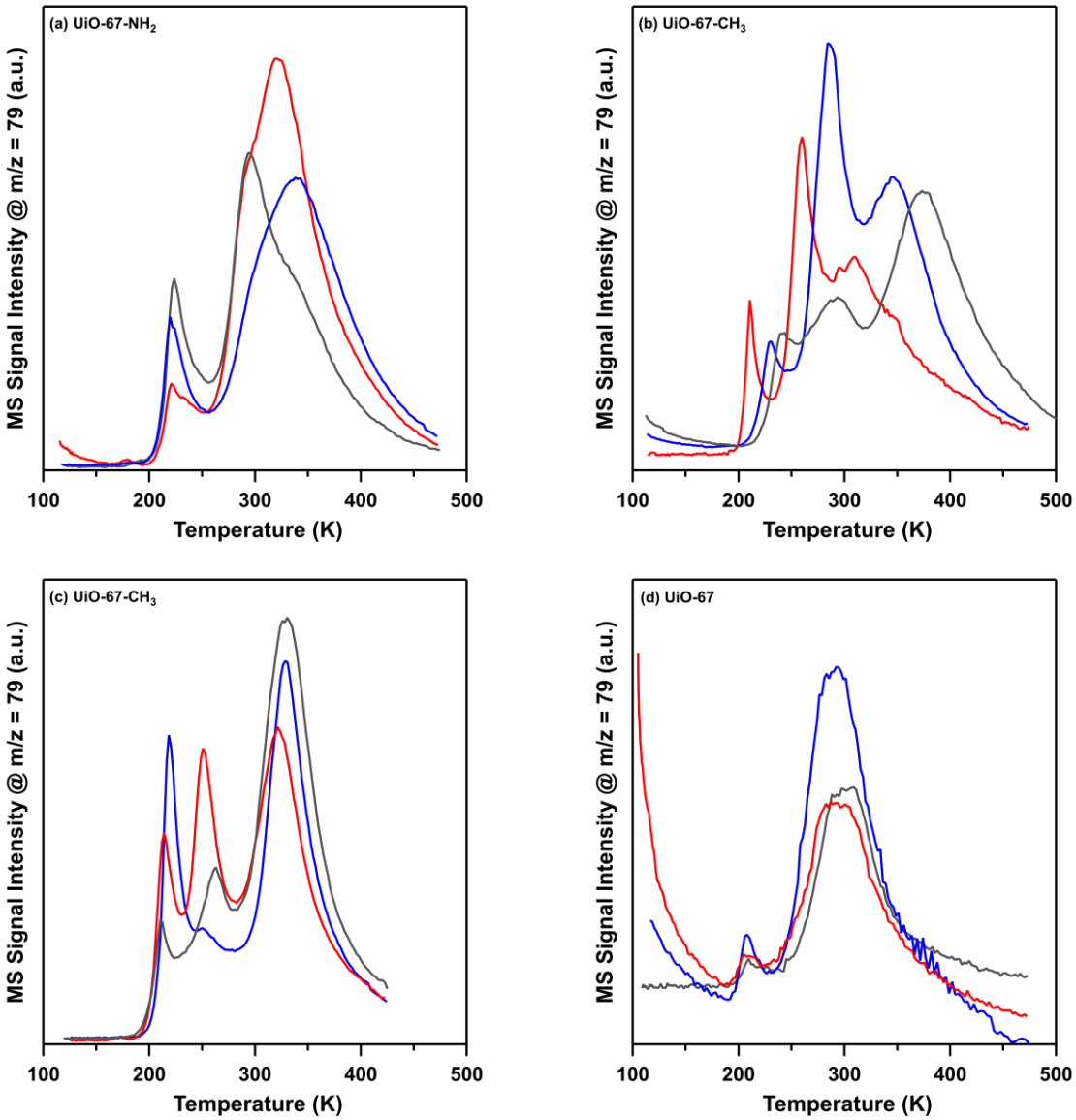

Figure S4: Thermal desorption profiles for (a) UiO-67-NH_2 activated to 473 K and (b) UiO-67-CH_3 activated to 473 K, (c) UiO-67-CH_3 activated to 423 K and (d) UiO-67 activated to 473 K. Red, blue and black traces represent unique sample batches individually introduced into the UHV chamber with no prior analyte exposure. UiO-67-NH_2 and UiO-67-CH_3 were exposed to 5000 L DMMP and UiO-67 was exposed to 1000 L DMMP. A total of 12 different MOF samples, from 12 different batches are represented.

Reproducibility of DMMP thermal desorption profiles was tested by exposing three unique samples of each of the MOFs, UiO-67-NH_2, UiO-67-CH_3 and UiO-67 to 5000 L DMMP (1000 L for UiO-67) and comparing the resulting TPD-MS desorption profiles. It can be seen from Figure S*4* that when UiO-67-NH_2 and UiO-67 are activated to 473 K, the position of the maximum temperature of desorption (T_{max}) for all sites are in good agreement. The variability in the intensity of the peaks is due to the number of sites available for binding between samples, which does not

significantly impact T_{max} for each site. However, when UiO-67-CH_3 samples were activated to 473 K, T_{max} varied between samples, which suggests that activation at 473 K may change this MOF. As a result, the UiO-67-CH_3 sample was activated to a lower temperature (423 K) and the resulting thermal desorption profile had a higher degree of reproducibility.

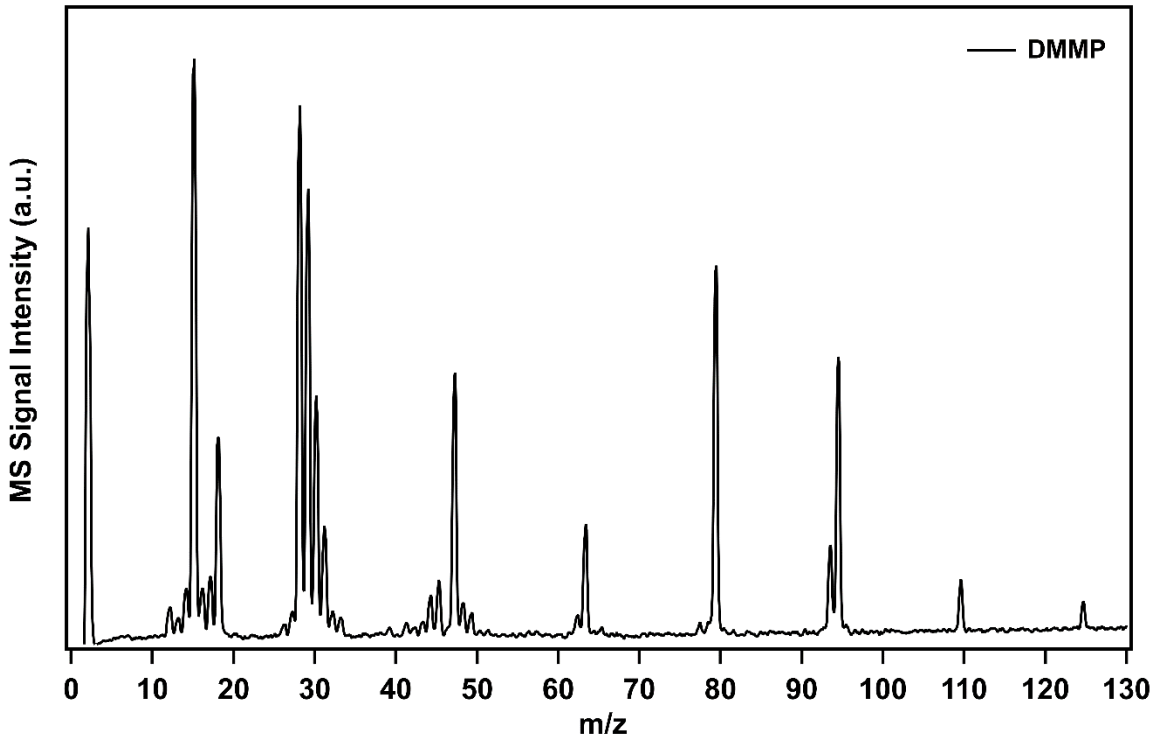

Figure S5. Full DMMP mass spectrum after purification via consecutative freeze-pump-thaw cycles.

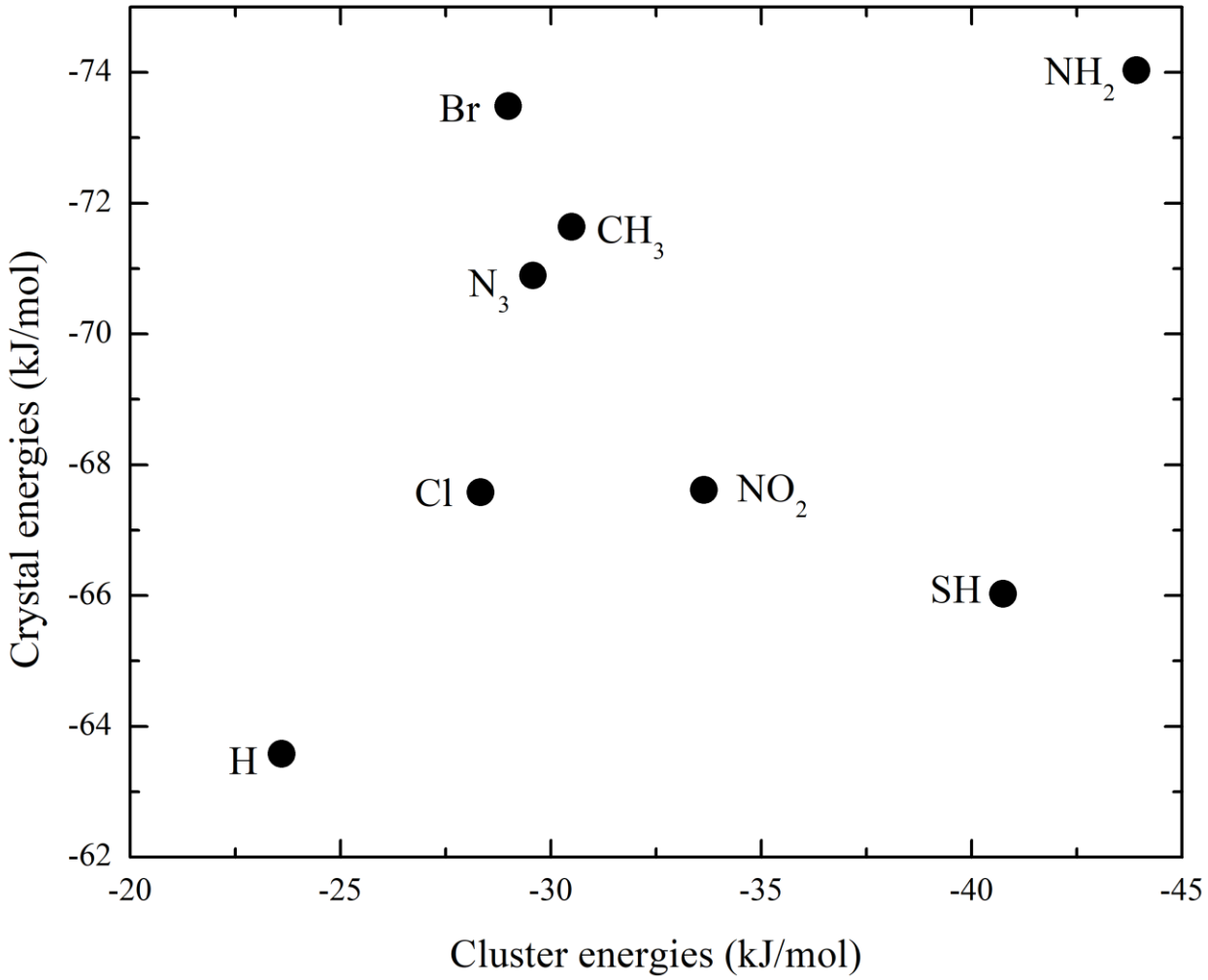

Figure S6: Comparison of cluster and crystal binding energies between DMMP and functionalized MOFs, as calculated from Orca and CP2K respectively. Only the strongest binding energy is shown.

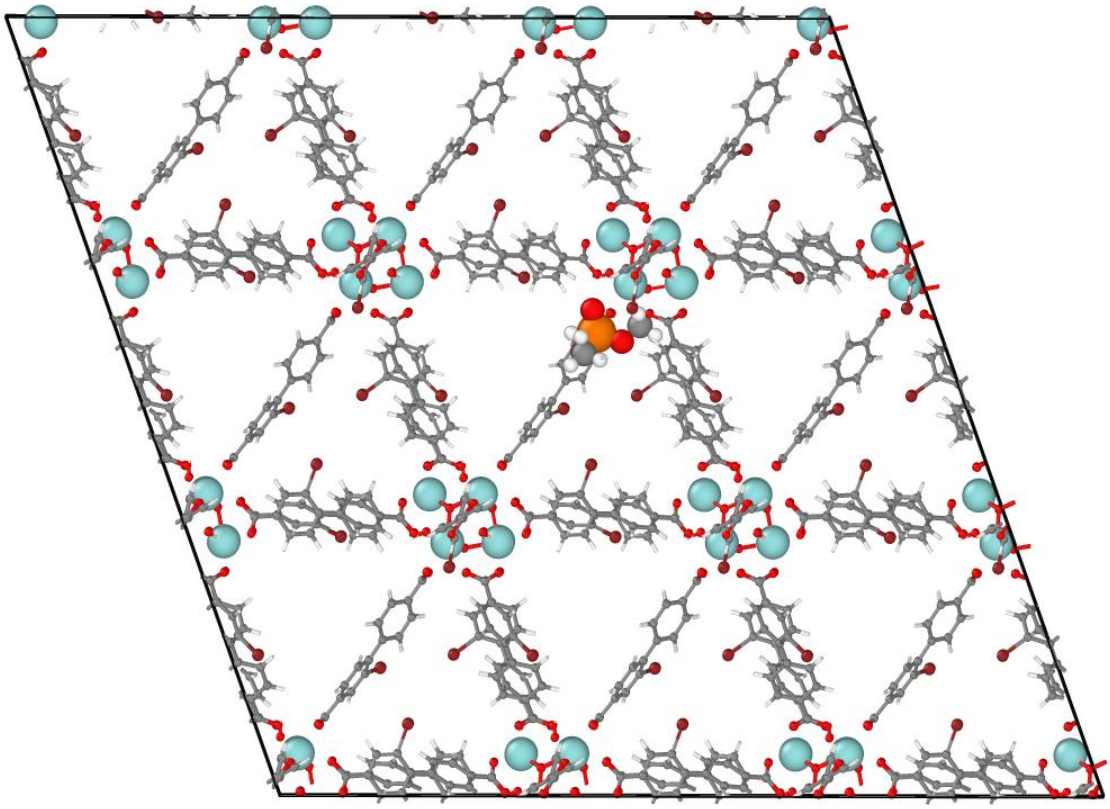

Figure S7. UiO-67-Br interaction with DMMP. Zr shown in light blue, oxygen shown in red, carbon shown in gray, bromine shown in burgundy, hydrogen shown in white.

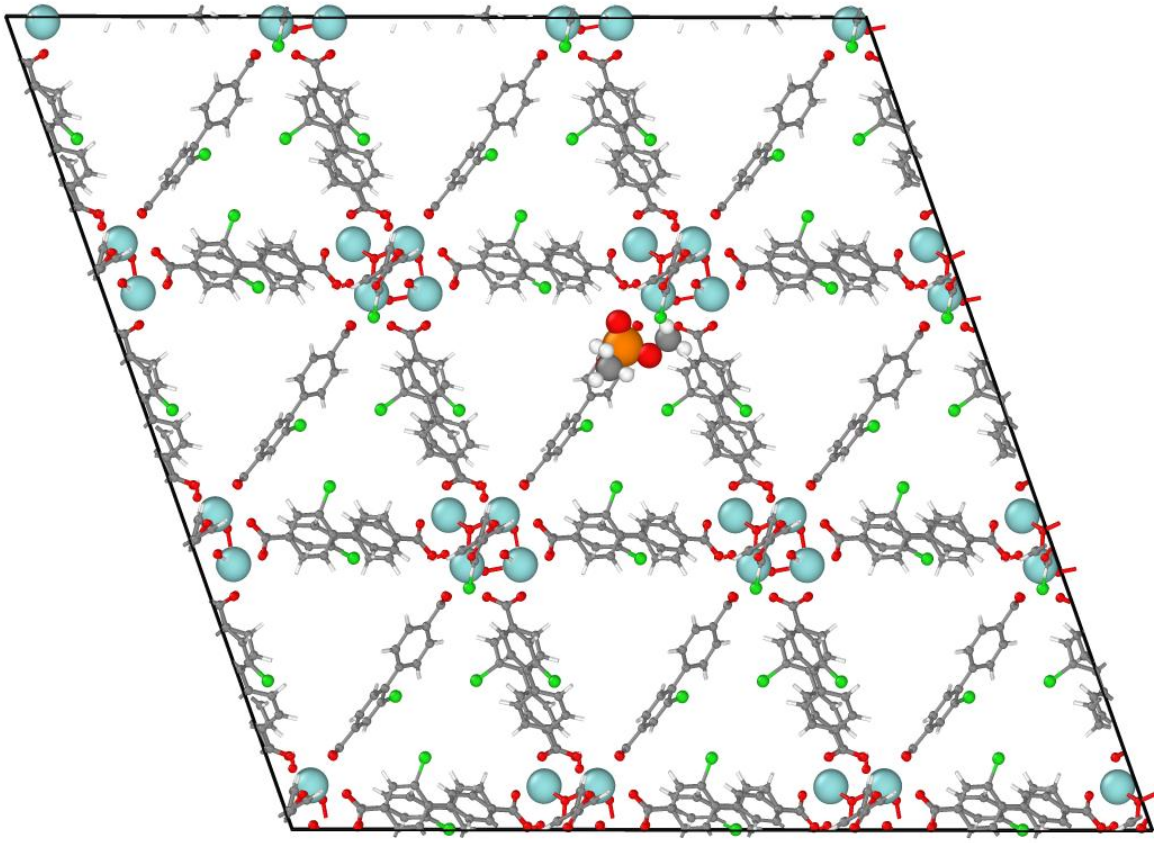

Figure S8. UiO-67-Cl interaction with DMMP. Zr shown in light blue, oxygen shown in red, carbon shown in gray, chlorine shown in lime green, hydrogen shown in white.

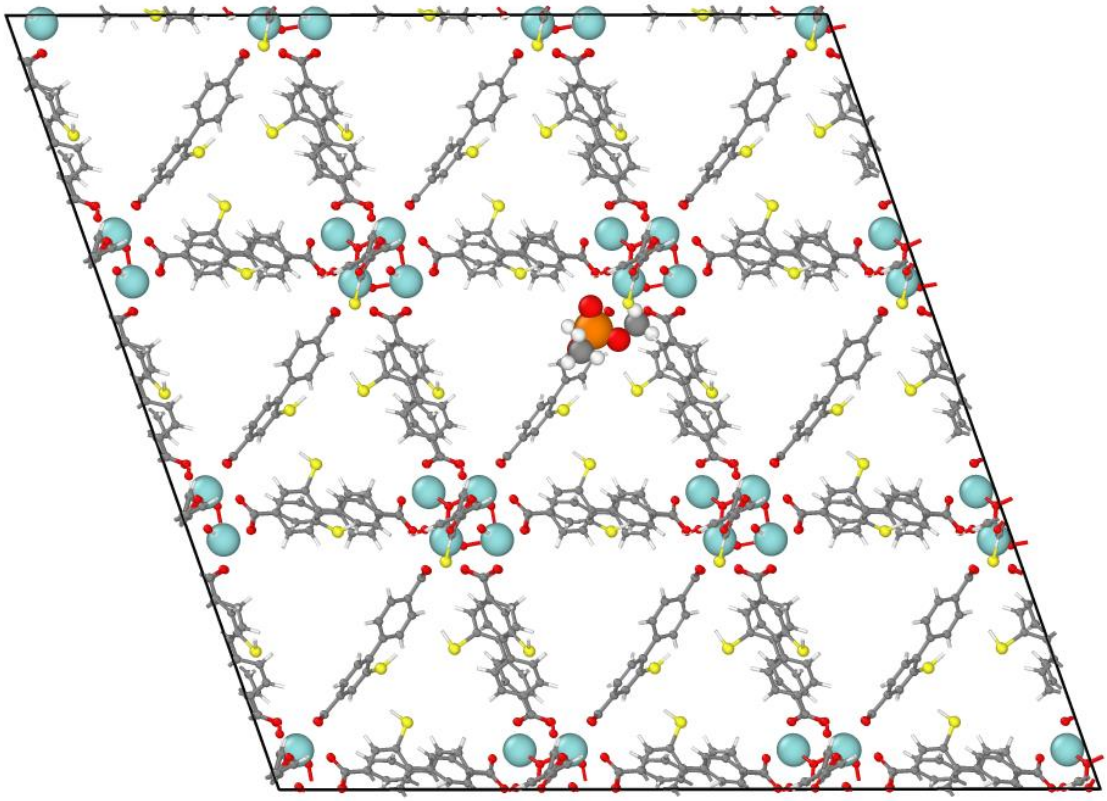

Figure S9. UiO-67-SH interaction with DMMP. Zr shown in light blue, oxygen shown in red, carbon shown in gray, sulfur shown in yellow, hydrogen shown in white.

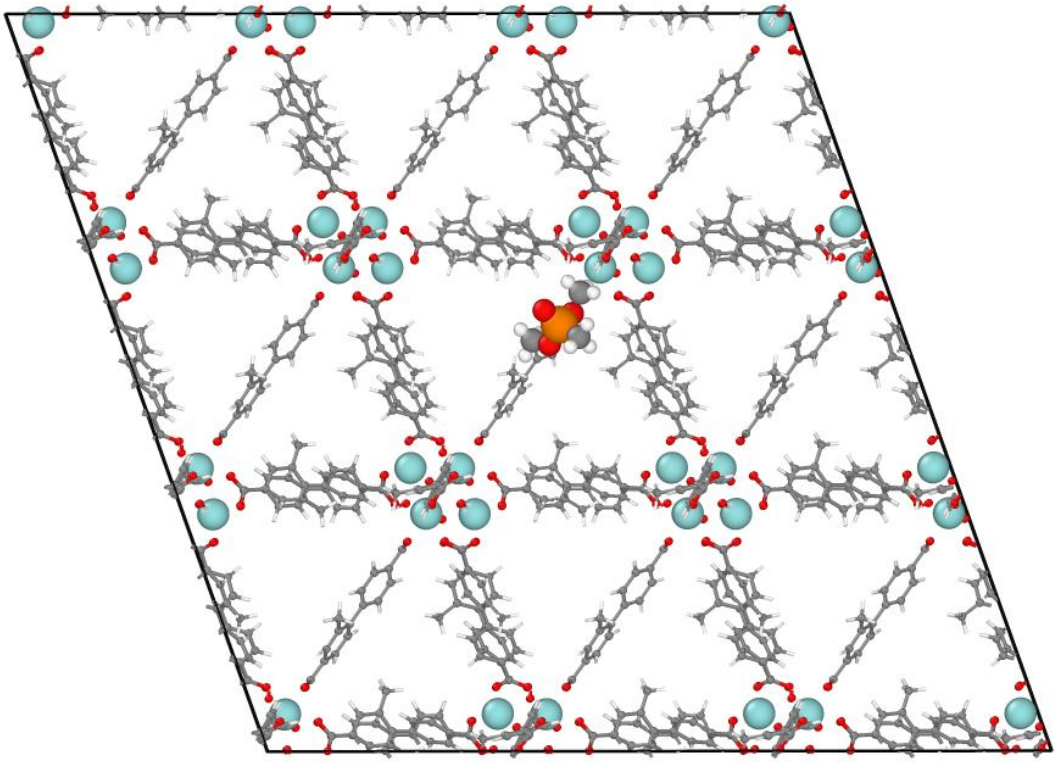

Figure S10. UiO-67-CH_3 interaction with DMMP. Zr shown in light blue, oxygen shown in red, carbon shown in gray, hydrogen shown in white.

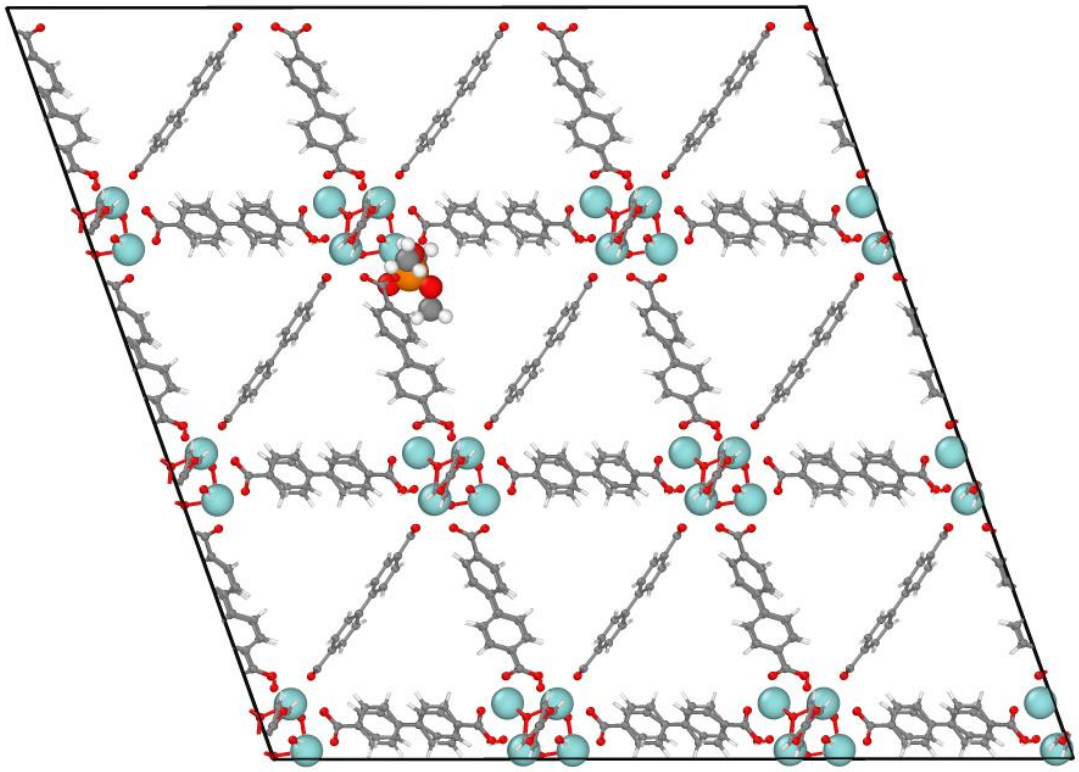

Figure S11. UiO-67 interaction with DMMP. Zr shown in light blue, oxygen shown in red, carbon shown in gray, hydrogen shown in white.

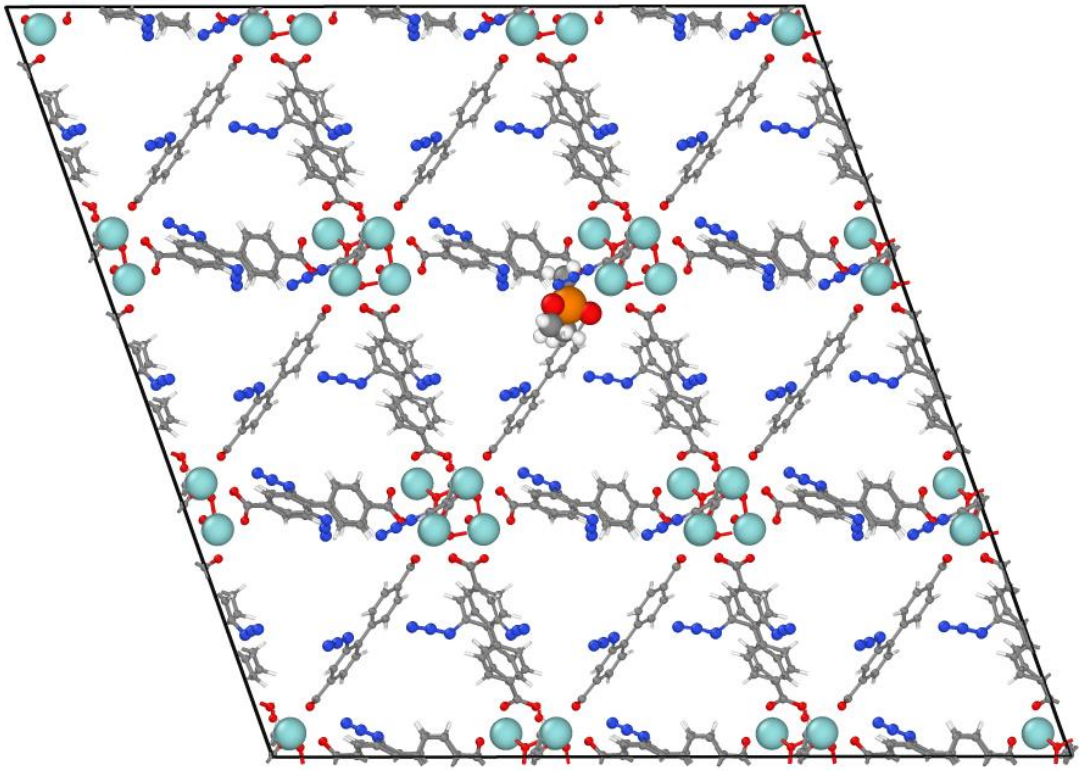

Figure S12. UiO-67-N_3 interaction with DMMP. Zr shown in light blue, oxygen shown in red, carbon shown in gray, nitrogen shown in blue, hydrogen shown in white.

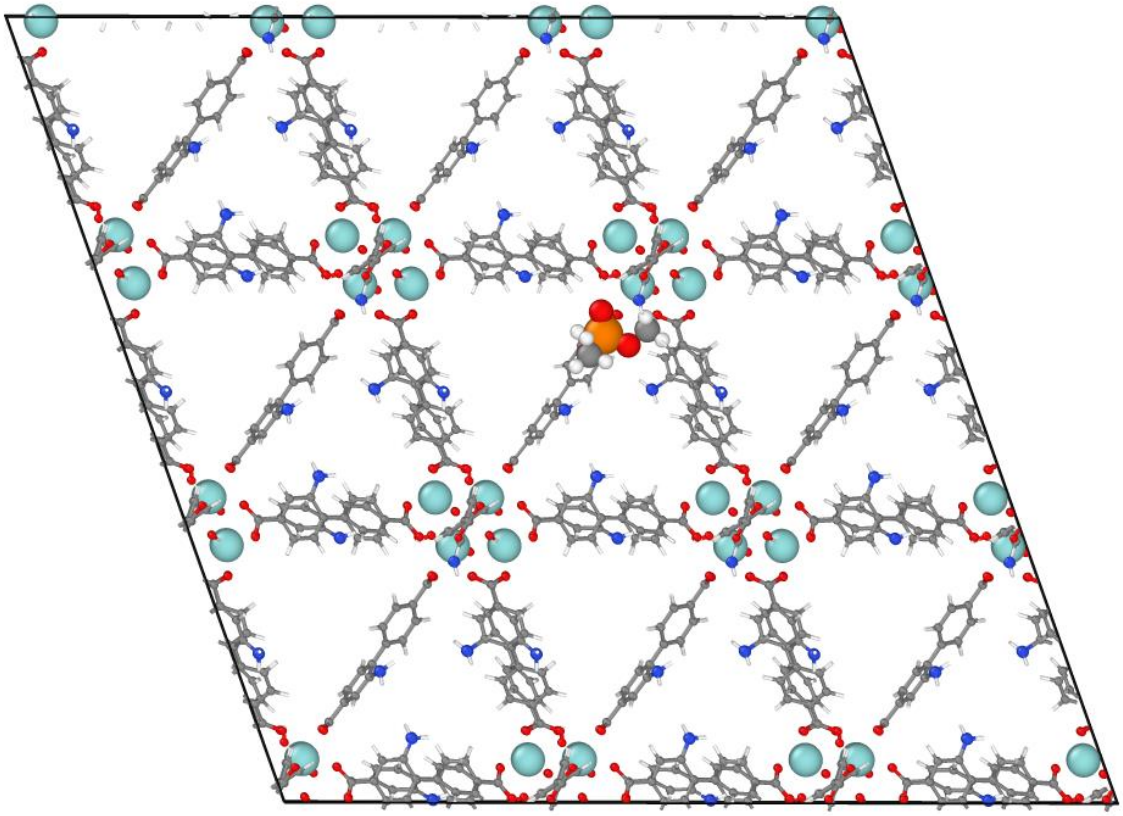

Figure S13. UiO-67-NH_2 interaction with DMMP. Zr shown in light blue, oxygen shown in red, carbon shown in gray, nitrogen shown in blue, hydrogen shown in white.

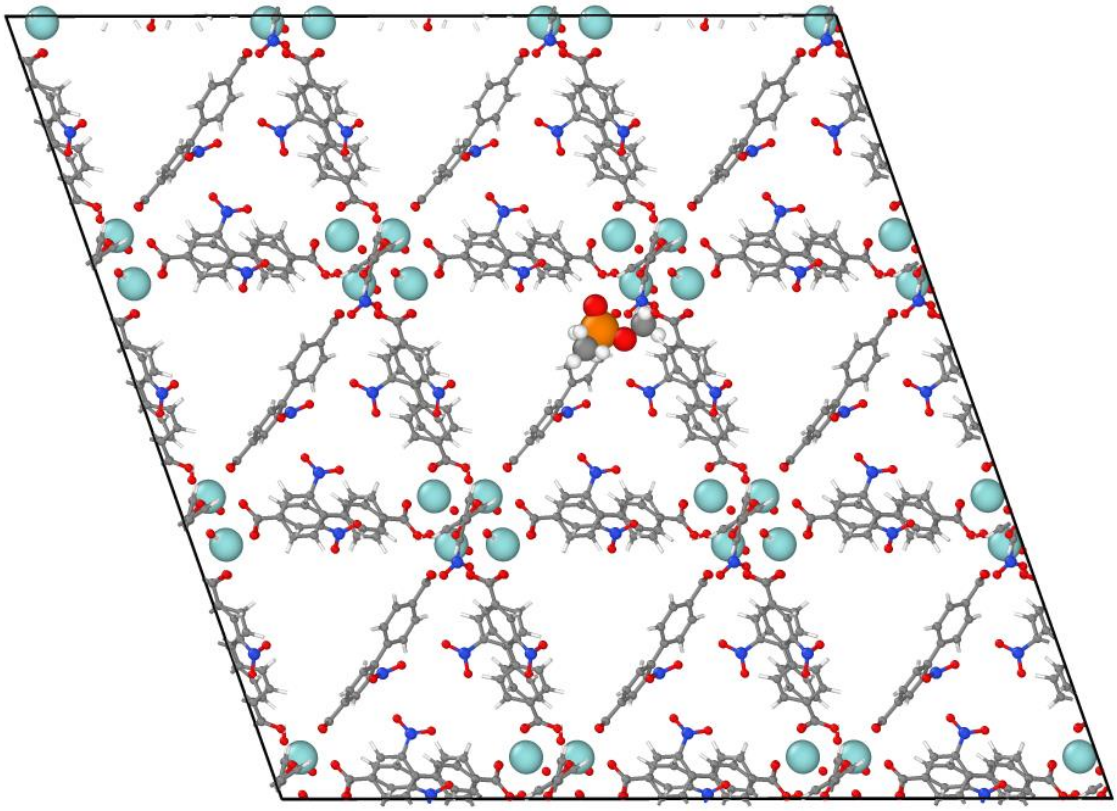

Figure S14. UiO-67-NO_2 interaction with DMMP. Zr shown in light blue, oxygen shown in red, carbon shown in gray, nitrogen shown in blue, hydrogen shown in white.

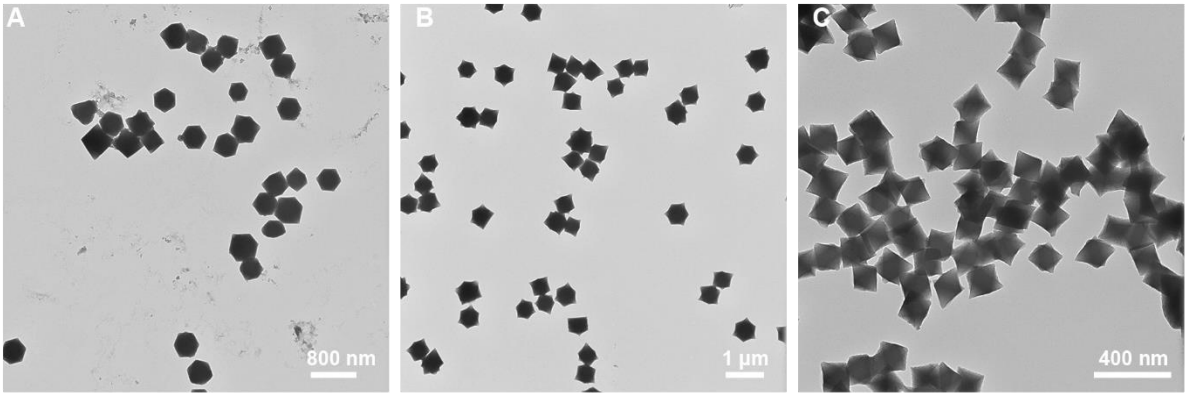

Figure S15. TEM images of (A) UiO-67 crystals, (B) UiO-67-CH_3 crystals and (C) UiO-67-NH_2 crystals.

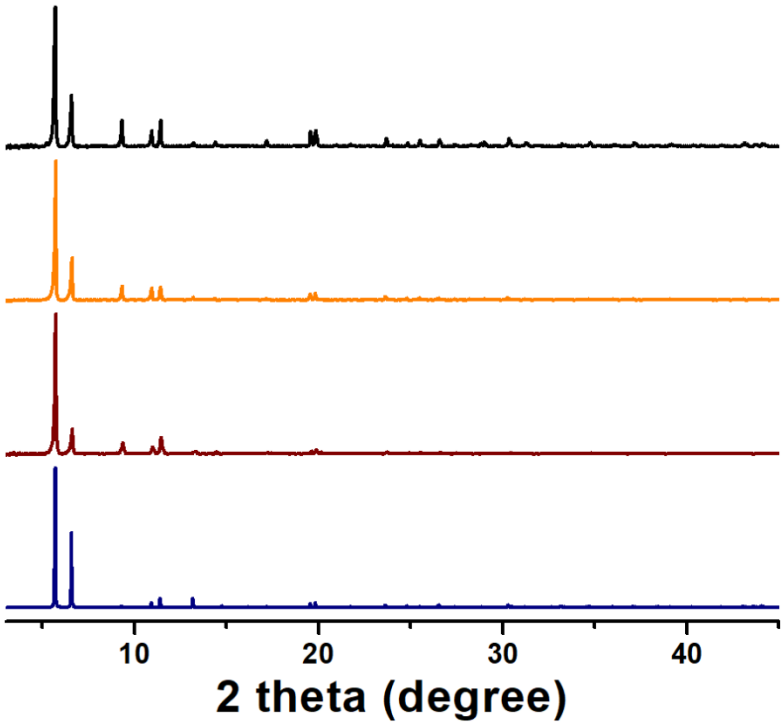

Figure S16. Powder X-ray diffraction patterns of as-synthesized UiO-67 (black), as-synthesized UiO-67-NH_2 (orange) and as-synthesized UiO-67-CH_3 (red) in comparison with simulated PXRD pattern based on the UiO-67 crystal structure (blue).

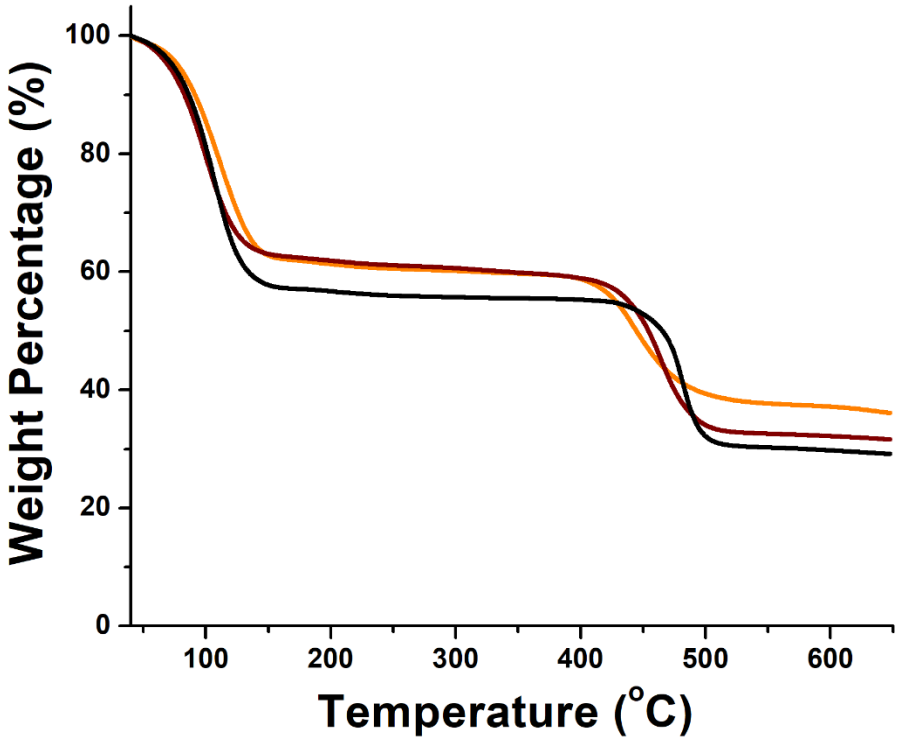

Figure S17. Thermogravimetric analyses of as-synthesized UiO-67 (black), UiO-67-CH_3 (red), and UiO-67-NH_2 (orange).

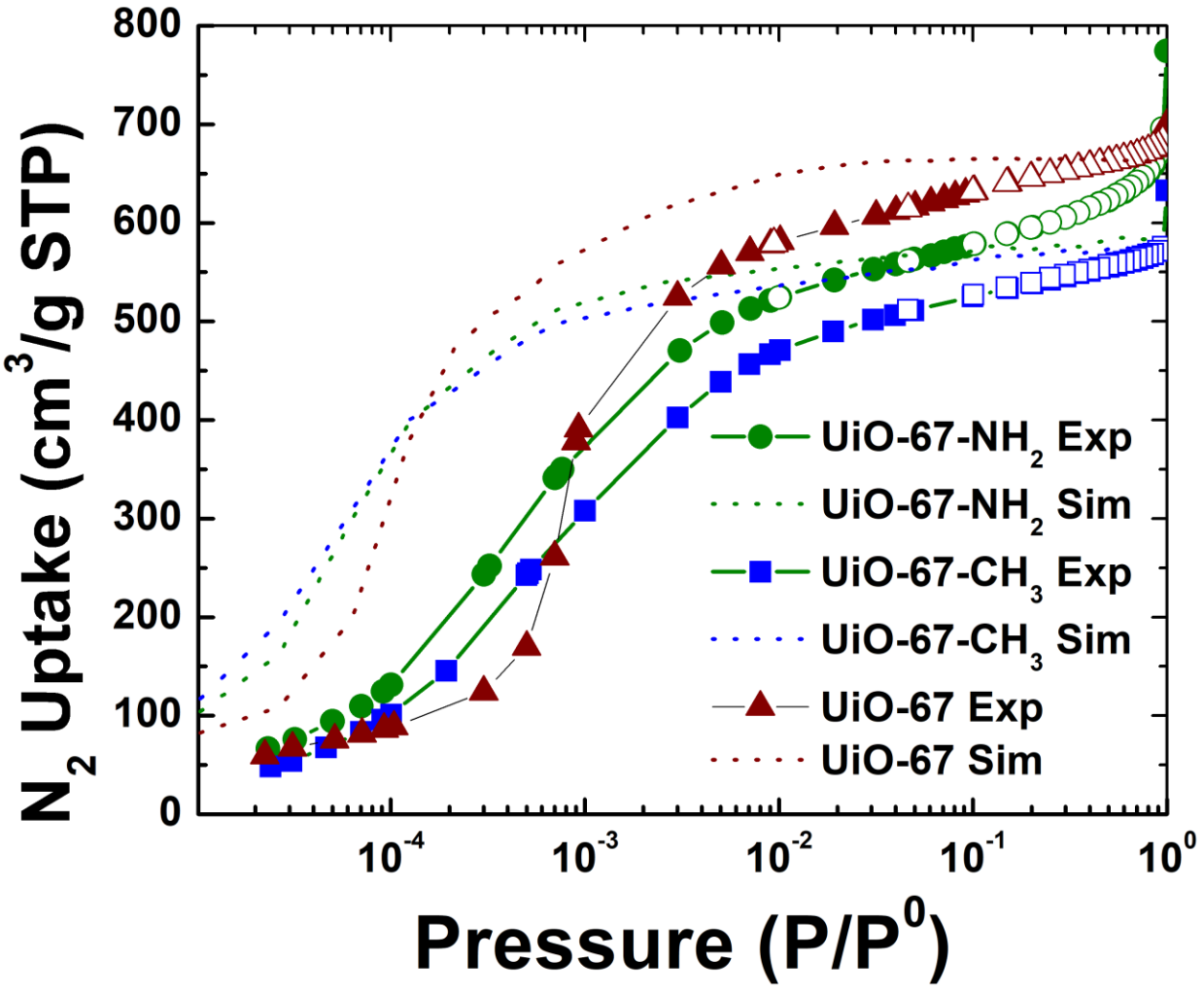

Figure S18. Nitrogen adsorption isotherms at 77 K from experiments (points) and simulations (lines). The model is too attractive at low to moderate pressures, but it correctly captures the behavior of the isotherms. There is no hysteresis in the experimental isotherms, as seen from agreement between adsorption (filled symbols) and desorption (open symbols). The model gives reasonable agreement at saturation.

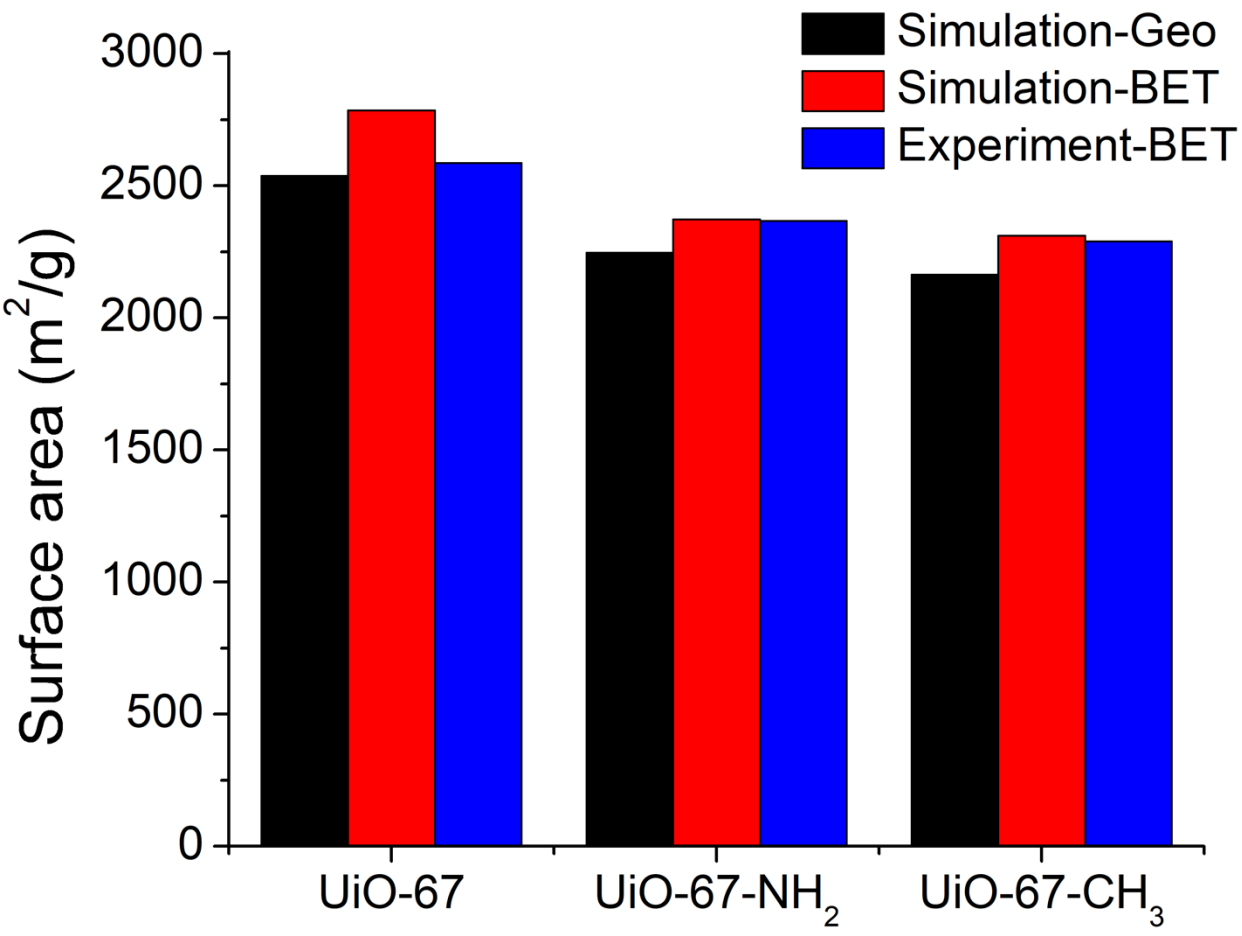

Figure S19. Surface areas for the synthesized MOFs computed from simulations and from experimental BET measurements based on N_2 isotherms at 77 K. The data shown as black bars were computed from a geometric algorithm involving rolling an argon atom over the surface of the MOF. The data shown as red bars were computed from applying the BET equation to simulated N_2 isotherms at 77 K (Figure S18). The blue bars represent BET surface areas from experimental N_2 isotherms at 77 K (Figure S18). The slight difference in geometric and BET surface areas is to be expected from different definitions of the surface area. Overall, the agreement is very good between the experiments and simulations.

The results of statistical analysis tabulated in Table S10 - Table S12 show that the models of adsorption for each MOF significantly differed from the mean. This is only one way of conducting a statistical analysis for non-linear models. Another way to examine the data for significant differences is by conducting an equivalence test, which directly compares the models to each other. Here, UiO-67-CH_3 was selected to be the reference model. For both analysis methods, α was set at 0.05. The results of this analysis are tabulated in Table S13 and Table S14. That a significant

result is observed in this analysis as well cements the assertion that there is a significant difference in DMMP adsorption based on the model developed here.

Table S10. Analysis of means found that the growth rate term of the models was significantly different from the mean for the methyl and unfunctionalized MOFs.

level	lower limit	estimate	upper limit	limit exceeded
UiO-67	1648	2705	2384	upper
UiO-67-CH_3	1783	1695	2249	lower
UiO-67-NH_2	1775	2064	2257	-

Table S11. Analysis of means found that the inflection points of the models were significantly different from the mean for all three of the models.

level	lower limit	estimate	upper limit	limit exceeded
UiO-67	0.002516	0.003635	0.002762	upper
UiO-67-CH_3	0.002529	0.002892	0.002749	upper
UiO-67-NH_2	0.002575	0.002283	0.002703	lower

Table S12. Analysis of means found that the asymptotes of the models were significantly different from the mean for all three models.

level	lower limit	estimate	upper limit	limit exceeded
UiO-67	147	162	152	upper
UiO-67-CH_3	147	143	152	lower
UiO-67-NH_2	147	145	152	lower

Table S13. Equivalence tests between the model for UiO-67-CH_3 and UiO-67 show that the growth rate and inflection points of the models were significantly different.

level	lower CL	ratio	upper CL	limit exceeded
growth rate	1.38	1.60	1.81	both
inflection point	1.21	1.26	1.30	upper
asymptote	1.12	1.13	1.15	-

Table S14. Equivalence tests between the model for UiO-67-CH_3 and UiO-67-NH_2 show that the growth rate and inflection points of the models were significantly different.

level	lower CL	ratio	upper CL	limit exceeded
growth rate	1.06	1.22	1.37	upper
inflection point	0.76	0.79	0.82	lower
asymptote	1.00	1.01	1.03	

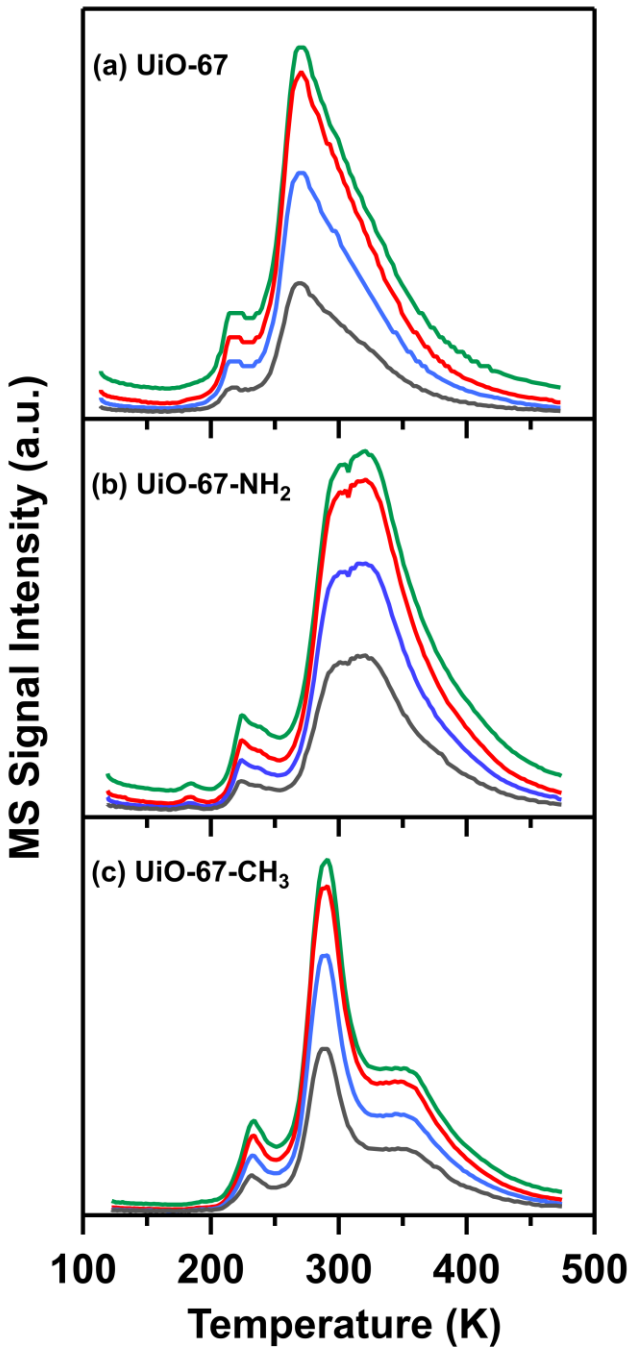

Figure S20. Mass spectra temperature profiles showing all mass fragments: m/z = 15 (green), m/z = 79 (red), m/z = 94 (blue) and m/z = 109 (gray). All DMMP fragments share similar profiles indicating molecular desorption of DMMP. Note: m/z = 109 was multiplied by 3 for improved resolution.

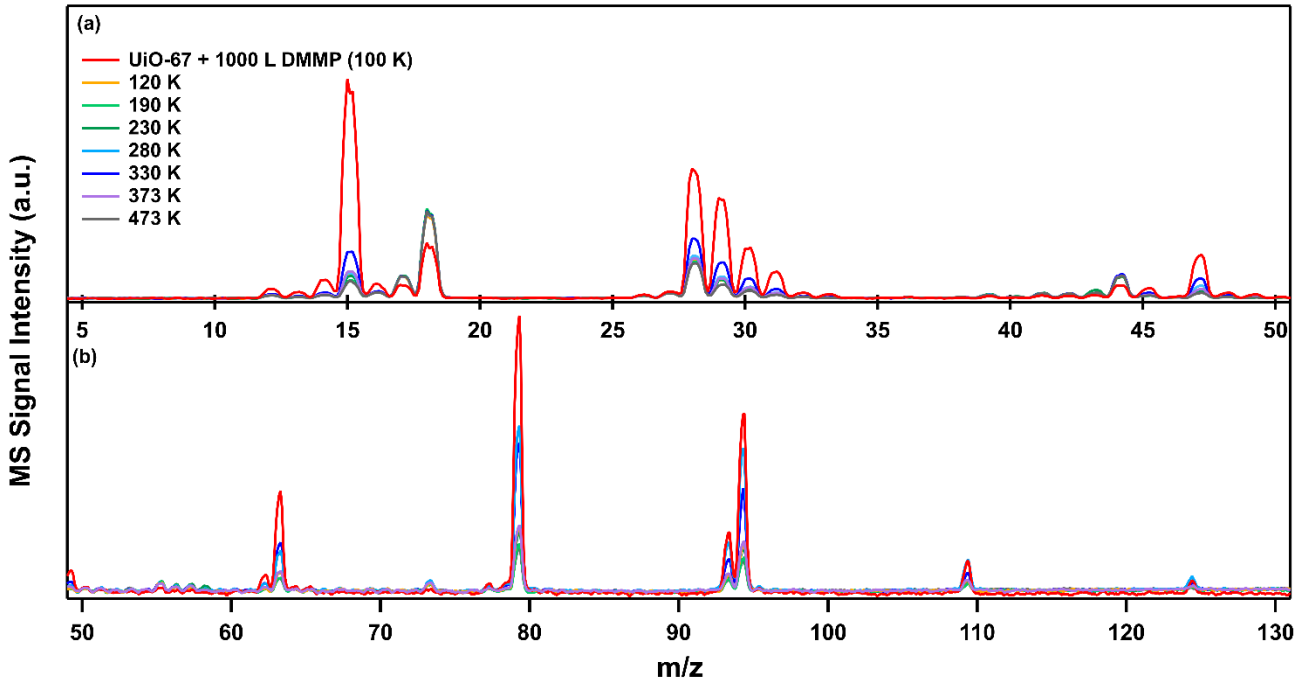

Figure S21. Full mass spectra of UiO-67 recorded during heating (100 K – 473 K) following exposure to 1000 L DMMP at 100 K showing: (a) mass range 5 – 50 amu and (b) 50 – 130 amu.

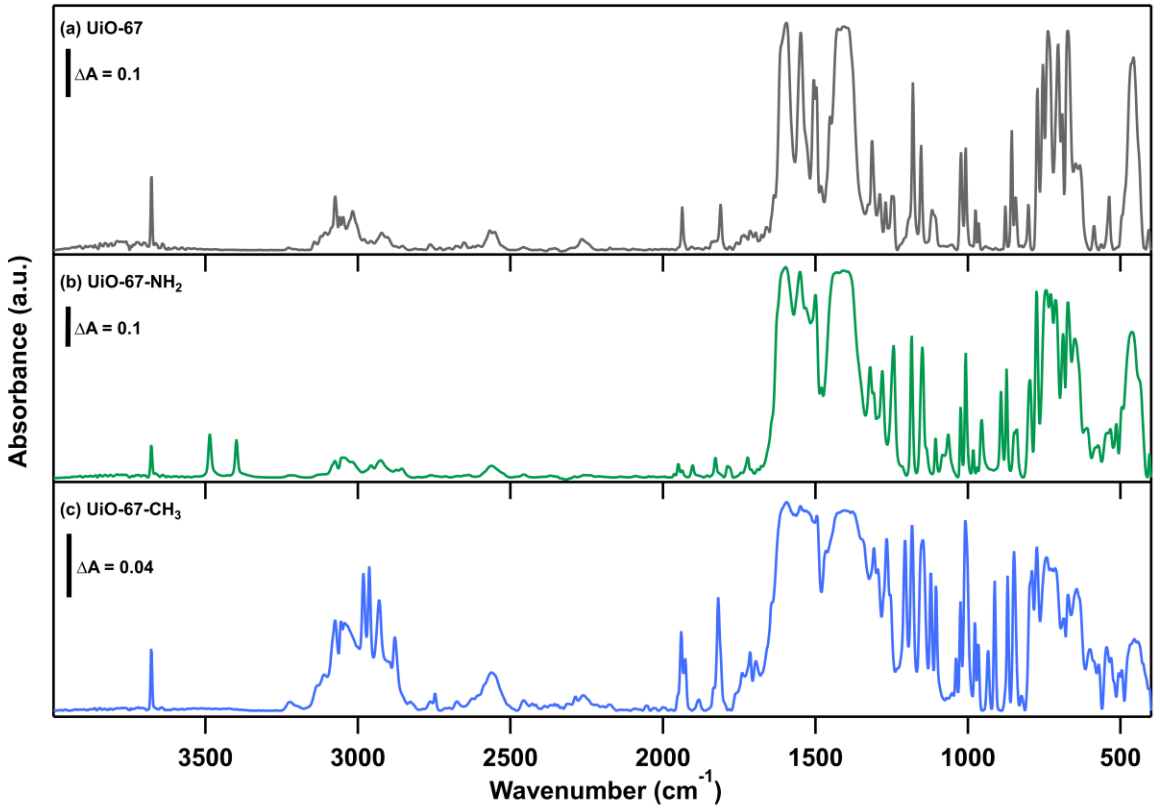

Figure S22. Full IR Spectra (400 – 4000 cm^{-1}) of clean UiO-67 MOFs prior to DMMP exposure: (a) UiO-67 (gray), (b) UiO-67-NH_2 (green), (c) UiO-67-CH_3 (blue). Baseline corrected spectra were taken at 100 K.

Differential Adsorption Concentrations

The differences in binding energies for DMMP in the UiO-67-NH_2, UiO-67-CH_3, and UiO-67 MOFs can give rise to equilibrium concentration differences in a stratified MOF. Assume a three-stratum MOF UiO-67-NH_2⊂UiO-67-CH_3⊂UiO-67 (inner most stratum MOF UiO-67-NH_2). The DFT calculated binding energies for DMMP in these MOFs are -74, -71, and -64 kJ/mol, respectively. Assuming a Boltzmann distribution and referencing to UiO-67 (differential binding energies of -10, -7, 0 kJ/mol, respectively) gives Boltzmann factors of 55.1 and 16.6 for UiO-67-NH_2 and UiO-67-CH_3, respectively. Thus, the concentration of DMMP in the UiO-67-NH_2 stratum should be 55.1 times larger than in UiO-67.

References

1. Neese, F., The ORCA program system. *Wiley Interdiscip. Rev.: Comput. Mol. Sci.* **2012,** *2*, 73-78.
2. Frigo, M.; Johnson, S. G., The Design and Implementation of FFTW3. *Proceedings of the IEEE* **2005,** *93*, 216-231.
3. VandeVondele, J.; Krack, M.; Mohamed, F.; Parrinello, M.; Chassaing, T.; Hutter, J., Quickstep: Fast and accurate density functional calculations using a mixed Gaussian and plane waves approach. *Comput. Phys. Commun.* **2005,** *167*, 103-128.
4. VandeVondele, J.; Hutter, J., An efficient orbital transformation method for electronic structure calculations. *J. Chem. Phys.* **2003,** *118*, 4365-4369.
5. Liu, C.; Luo, T.-Y.; Feura, E. S.; Zhang, C.; Rosi, N. L., Orthogonal Ternary Functionalization of a Mesoporous Metal–Organic Framework via Sequential Postsynthetic Ligand Exchange. *JACS* **2015,** *137*, 10508-10511.
6. Yuan, S.; Zou, L.; Li, H.; Chen, Y.-P.; Qin, J.; Zhang, Q.; Lu, W.; Hall, M. B.; Zhou, H.-C., Flexible Zirconium Metal-Organic Frameworks as Bioinspired Switchable Catalysts. *Angew. Chem. Int. Ed.* **2016,** *55*, 10776-10780.
7. Vanduyfhuys, L.; Vandenbrande, S.; Verstraelen, T.; Schmid, R.; Waroquier, M.; Van Speybroeck, V., QuickFF: A program for a quick and easy derivation of force fields for metal-organic frameworks from ab initio input. *J. Comput. Chem.* **2015,** *36*, 1015-1027.
8. Kresse, G.; Furthmüller, J., Efficient iterative schemes for ab initio total-energy calculations using a plane-wave basis set. *Phys. Rev. B* **1996,** *54*, 11169-11186.
9. Kresse, G.; Furthmüller, J., Efficiency of ab-initio total energy calculations for metals and semiconductors using a plane-wave basis set. *Computational Materials Science* **1996,** *6*, 15-50.
10. Kresse, G.; Hafner, J., Ab initio molecular-dynamics simulation of the liquid-metal--amorphous-semiconductor transition in germanium. *Phys. Rev. B* **1994,** *49*, 14251-14269.
11. Kresse, G.; Hafner, J., Ab initio molecular dynamics for liquid metals. *Phys. Rev. B* **1993,** *47*, 558-561.